

Gennaro H. Crescenti, Jeffrey R. French, and Timothy L. Crawford  
Air Resources Laboratory Field Research Division  
National Oceanic and Atmospheric Administration  
Idaho Falls, Idaho

Douglas C. Vandemark  
Laboratory for Hydrospheric Processes  
NASA / Goddard Space Flight Center  
Wallops Island, VA

## 1. INTRODUCTION

A small single-engine research aircraft has been used in numerous air-sea interaction research studies to investigate the spatial variation of both the marine atmospheric boundary layer and the ocean surface wave field. The integrated instrument suite of *in situ* sensors carried by a LongEZ (registration N3R) airplane is used to measure mean properties of the atmosphere as well as turbulent fluxes of heat, moisture, and momentum. These data are coupled with remote sensor measurements of the ocean surface, such as sea surface temperature, wave height, length, slope, and phase. This integrated measurement platform is a powerful tool to directly examine mass, momentum and energy exchange processes occurring across the air-sea interface.

## 2. AIRCRAFT

Over the last ten years, N3R (Fig. 1) has been used in a number of air-sea interaction research studies (Crawford et al. 1993, Crescenti et al. 1999; Vogel and Crawford 1999; French et al. 2000; Mourad et al. 2000; Vandemark et al. 2001). N3R is set apart from other airborne measurement platforms for a number of reasons.



Fig. 1. N3R in flight during a research mission.

The LongEZ was designed in the early 1980's as a high-performance sport aircraft. N3R is a custom-built aircraft licensed by the Federal Aviation Administration (FAA) under an experimental amateur-built airworthiness category. It is a safe and reliable aircraft with exceptional performance characteristics. The differences of N3R from that of other single-engine aircraft are visually apparent. Unlike most aircraft that are constructed with metal, N3R is fabricated from a lighter and stronger fiberglass and foam composite. Another important difference is that the engine is mounted on the rear of the airframe. The large main laminar-flow wing is set back further than that of conventional aircraft. Vertical winglets found on either end of the main wing enhance aircraft lift. A smaller second wing (canard) is found near the nose of the aircraft. This forward lifting surface is designed to increase aircraft stability and to prevent the main wing from stalling.

An important characteristic of an aircraft with a pusher engine and a canard is that it responds to turbulence far less than conventional aircraft with the same wing loading (weight per unit area). Since the canard contributes to both lift and stability, it can be heavily loaded relative to the main wing. For conventional aircraft with a rear-mounted elevator, an upward wind gust will tend to make the aircraft pitch up. This increases the lift generated by the wings and amplifies the aircraft response to an upward wind gust. In contrast, canard aircraft have their elevators forward of their center of gravity. The same upward wind gust will push the canard elevator up which results in a compensating downward pitch response. Aircraft pitch response to either upward or downward wind gusts is opposed to the gust direction, thus giving canard-type aircraft their superior turbulent response characteristics.

A canard aircraft is also stall-resistant. As the angle of attack on the airplane is increased, the canard loses lift before the main wing. This causes the nose to drop, which decreases the angle of attack, thereby providing automatic stall recovery without allowing the main wing to stall.

The unique aerodynamic design features of N3R makes it ideally suited for making high-fidelity turbulence measurements with minimal flow distortion at low altitudes ( $\sim 10$  m) and slow aircraft flight speeds ( $\sim 50$  m s<sup>-1</sup>). The small low-drag airframe and rear-mounted pusher engine have clear advantages for minimizing flow distortion and exhaust contamination (Crawford and Dobosy 1992). Instruments mounted on the aircraft nose avoid flow distortion, engine vibration, and engine exhaust. On N3R,

---

Corresponding author address: Gennaro H. Crescenti,  
U.S. Dept. Commerce / NOAA, Air Resources Laboratory  
1750 Foote Drive, Idaho Falls, ID 83402; e-mail:  
jerry.crescenti@noaa.gov

the wind measurement probe is five wing-widths (chord lengths) ahead of the canard. The resulting flow distortion is extremely low compared to other aircraft (Crawford et al. 1996).

The utility N3R is illustrated by its impressive specifications and performance (Table 1). There are few aircraft that will carry its own weight as payload. Typically, N3R will fly a research mission at  $50 \text{ m s}^{-1}$  consuming fuel at a rate of only  $15 \text{ l hr}^{-1}$ . Its fast cruise speed and long-range allow it to reach anywhere in the world. Because of its classification under FAA's experimental category, modifications can be made easily. N3R has been modified for scientific research with a larger engine, redundant high-output alternators, extended fuel tanks, and hard-points and port holes for instrument mounting. Fiberglass construction allows flexibility in modifying the airframe to mount sensors and instrument pods.

**Table 1.** N3R specifications.

Engine	Lycoming O-360
Seats	2
Electrical	12 vdc / 65 amp
Fuselage Length	5.0 m
Wing Span	8.5 m
Wing Area	$10 \text{ m}^2$
Canard Span	3.7 m
Canard Chord	0.38 m
Propeller Diameter	1.80 m
Weight (empty)	430 kg
Payload	370 kg
Fuel Capacity	300 kg
Range	3800 km
Ceiling	8000 m
Endurance	10 - 18 hr
Cruise Speed	$90 \text{ m s}^{-1}$
Stall Speed	$25 - 30 \text{ m s}^{-1}$
Fuel Use - $50 \text{ m s}^{-1}$	$11 \text{ kg hr}^{-1}$
Fuel Use - $90 \text{ m s}^{-1}$	$20 \text{ kg hr}^{-1}$

### 3. INSTRUMENTATION

#### 3.1 Wind Sensing System

The center piece of the N3R instrumentation package is the "best" aircraft turbulence (BAT) probe (Fig. 2). This device was designed, tested, and built as a result of a collaboration between NOAA's Air Resources Laboratory (ARL) and Airborne Research Australia (ARA) (Crawford and Dobosy 1992; Hacker and Crawford 1999). The housing consists of a 15-cm diameter carbon-fiber hemisphere mounted on a tapered carbon-fiber cone. The housing and cone are mounted on a roughly 3-m long cylinder protruding forward from the nose of the aircraft. The housing contains four solid-state pressure sensors used to measure differential (three) and static (one) pressure from nine pressure ports symmetrically located on the hemisphere. The nominal accuracy of these sensors is  $\pm 0.05 \text{ hPa}$  with a response of  $\sim 1 \text{ KHz}$ . These measurements provide the pressure distribution over the housing from which the relative air velocity may be computed.



**Fig. 2.** BAT probe and GPS antenna. The small round disk forward of the antenna is a LI-COR PAR sensor.

Two global positioning systems (GPS) are incorporated. A dual-frequency Ashtech GPS antenna is mounted on the tapered cone of the BAT probe just aft of the housing. By using differential GPS (DGPS) correction techniques, aircraft position can be measured to within several centimeters relative to a fixed point and ground velocity can be computed to an accuracy of roughly  $2 \text{ cm s}^{-1}$  in the horizontal and better than  $1 \text{ cm s}^{-1}$  in the vertical. These data are acquired at a rate of  $5 \text{ Hz}$ . Three orthogonally-mounted accelerometers contained in the BAT housing are used to augment the GPS position and velocity data to a frequency of  $50 \text{ Hz}$ .

Aircraft attitude (pitch, roll, and heading) is measured using a Trimble Advanced Navigation System (TANS) vector GPS. The TANS-vector consists of four antennas mounted on the BAT probe housing, on both wings, and the rear of the cockpit. Using carrier-phase techniques, the position of three antennas is measured relative to a master antenna. Manufacturer specified accuracy for aircraft attitude given the geometry of N3R is  $0.05^\circ$ . The TANS-vector GPS acquires attitude data at a maximum rate of  $10 \text{ Hz}$ . By differencing measurements acquired by accelerometers in the BAT probe housing and by three accelerometers mounted on the aircraft centerline in the back of the fuselage, the frequency range for aircraft pitch and heading are extended up to  $50 \text{ Hz}$ . Similarly, the frequency can be extended to  $50 \text{ Hz}$  for aircraft roll by differencing two accelerometers mounted on the wings. This "blending" technique of aircraft position, velocity, and attitude from data acquired by GPS and accelerometers is described by Crawford and Dobosy (1992).

Calibration of the differential pressure sensors is accomplished using a Mensor 4040 digital pressure transducer. The Mensor transducer and the instrument sensors are connected in parallel to a syringe that is used to adjust the pressure applied to both the sensors and calibration standard. The y- and z-axis sensors (lateral and vertical, respectively) are designed to respond to differential pressure of  $\pm 15 \text{ hPa}$  corresponding to an output of  $\pm 5 \text{ V}$ . The x-axis sensor (longitudinal) ranges from  $0$  to  $28 \text{ hPa}$  with a corresponding output of  $\pm 5 \text{ V}$ .

The accelerometers are calibrated by tipping the devices to known angles and calculating the contribution due to gravity as a function of angle. It is possible to produce a calibration curve over the entire range of the

device by making measurements over several angles.

The Ashtech and TANS-vector GPS are not calibrated per se, but checks are incorporated to ensure the data are within tolerance levels. For example, aircraft velocity data should be zero when N3R is parked on the tarmac. Data from previous experiments shown a mean velocity of zero, with a standard deviation of 1 to 2 cm s<sup>-1</sup>. Spectra indicate the noise in the velocity data appears white (random).

### 3.2 Temperature and Humidity Sensors

Three different probes are used to measure air temperature. A slow-response multi-element linear thermistor provides low frequency (1 Hz) temperature measurements. This sensor is mounted within the center-hole, or design stagnation point (DSP), port on the BAT hemisphere. A fast-response (~20 Hz) 0.13-mm micro-bead thermistor is also mounted inside the DSP port. The recovery factor for micro-bead thermistor is 0.82. The calculation of the correction factor due to compression is simpler than for more conventional temperature probes because of the location of the sensors within the DSP. A third sensor is the fast ultra-sensitive temperature (FUST) probe (French et al. 2001). This sensor is a Cu-Co 0.025-mm thermocouple and has a response time of better than 20 ms. The probe is mounted on a post below the hemisphere of the BAT probe.

The slow-response thermistor is calibrated against an accurate mercury-bulb thermometer at various temperatures. This method provides a reasonably stable calibration to an accuracy of ~1 °C. The micro-bead thermistor is calibrated in flight. Calibration curves are based on output from the slow-response thermistor. Generally, the micro-bead thermistor is highly correlated with the slow-response probe with correlation coefficients exceeding 0.96. Yet, there exist regions where deviations occur. In general, these areas consist of greater turbulence (we would expect deviations due to differences in time response) and/or maneuvers that affect the recovery factors of the sensors (due to their location within the housing). In addition, these thermistors are also calibrated in a well controlled water bath over a range of temperatures.

Humidity is measured with two different sensors. A chilled mirror sensor provides dew point temperature. This sensor has a relatively long response time (as much as a few seconds). An ARL designed and built fast-response (~50 Hz) open-path infrared gas analyzer (IRGA) measures the attenuation of light due to CO<sub>2</sub> and H<sub>2</sub>O through a known path (Auble and Meyers 1992).

The IRGA is calibrated by placing the sensor inside a chamber with known concentrations of CO<sub>2</sub> and H<sub>2</sub>O. Water vapor calibration is conducted for absolute humidity between 5 and 30 g m<sup>-3</sup>. A quadratic equation is used to fit the curve between 5 g m<sup>-3</sup> and 18 g m<sup>-3</sup>. Values outside this range are subject to larger errors.

### 3.3 Other Atmospheric Sensors

Three sets of radiometric sensors mounted on N3R measure upwelling and downwelling (with respect to the aircraft) radiation. A Radiation and Energy Balance

Systems Q\*7.1 net radiometer provides measurements of both long and shortwave radiation. Upward looking and downward looking LI-COR photosynthetically active radiation (PAR) sensors measure the incoming and reflected portion of the visible solar spectrum, respectively. Upward and downward looking Everest Interscience 4000.4GL and 4000.4GXL infrared (IR) radiometers are used to measure sky and sea surface temperature (SST), respectively. The downward looking IR radiometer has a response time of 20 ms and a reported accuracy of ±0.5 °C. Laboratory testing showed that accurate SST measurements (< 0.2 °C) could be improved if the body temperature of the probe could be kept at a constant temperature. A temperature controller and an insulated flexible heater were purchased. The flexible heater was wrapped around the body of the IR sensor and encased with a layer of insulation. A second-order polynomial calibration curve has also replaced a linear regression.

### 3.4 Ocean Surface Remote Sensors

A laser altimeter array and a nadir-pointing 36-GHz (Ka-band) scatterometer are used to determine long and short wave characteristics, respectively, of the sea surface (Fig. 3). The data obtained from these remote sensors is unique in that it provides wave information from small capillary waves to long swells coupled with wind stress and turbulence measurements acquired by the BAT probe in the atmospheric surface layer.



**Fig. 3.** A Riegl laser altimeter (left) and NASA Ka-band scatterometer (right).

An array of Riegl LD90 downward looking laser altimeters is designed to measure the sea surface profile and the one- and two-dimensional slopes of intermediate scale waves on the order of 1 to 10 m. The laser array consists of three downward looking lasers mounted in an equilateral triangle with 1-m separation. Two are mounted under either wing while the third is mounted in a pod below the aircraft. These lasers simultaneously measure sea surface height at points about the 1-m diameter circular footprint of the radar scatterometer. The circular footprint of each laser is about 7.5 mm in diameter at an altitude of 15 m. The two lasers mounted in either wing operate with a pulse repetition frequency of 2 KHz while the third laser

located in the pod operates at a frequency of 12 KHz. The individual pulses are averaged down to a rate of 150 Hz to reduce noise resulting in 13 pulses per scan for the 2-KHz lasers and 80 pulses per scan for the 12-KHz laser. The lasers output distance, normalized amplitude of the returned pulse, and number of valid returns. The focal length of the lasers was set to 15 m providing a nominal accuracy of  $\pm 2$  mm. Given the laser measurements and aircraft attitude at any given time, matrix multiplications yield the vector normal to the sea surface plane. Other derived products include significant wave height, dominant wavelength of the wind sea, and the slope variance of the measured 2D probably density function. This last parameter is denoted as the mean square slope (mss) of long waves. The mss can be considered as the slope variance associated with intermediate scale gravity waves.

Along-track changes in the integrated roughness of short ocean waves on the order of 2 to 100 cm are determined using a nadir-pointing 36-GHz (8.3 mm) continuous wave scatterometer (Vandemark et al. 2001). This sensor is used to infer the short wave characteristics by relating backscatter intensity to the surface slope variance. The two-antenna remote sensor has a two-way, 3-dB beamwidth of  $4.1^\circ$  which corresponds to a 1.1-m footprint diameter at 15 m. Coincident laser altimeter measurements provide the precise range information for computation of the normalized radar cross section which is used in turn to derive the total mean square slope. The radar/laser combination leads to high fidelity observations of the long-wave, short-wave hydrodynamic modulation transfer function.

#### 4. DATA ACQUISITION SYSTEM

The N3R data acquisition system consists of a modified personal computer (PC) powered by a Intel Celeron 600 MHz processor. The PC is mounted on the floor of the backseat of N3R. The data acquisition programs run on top of the MS-DOS 6.22 operating system.

Analog sensor signals are digitized using remote modules (REMs) designed by ARA. Two REMs are currently used in the data acquisition system: One in the tapered cone of the BAT probe and another in an auxiliary electronics box next to the PC. Each REM consists of two 16-bit, 8-channel analog-to-digital (A/D) converters. The analog input voltage ranges from -5 to +5 volts, translating to a digital resolution of 0.15 mV. The incoming analog signals are filtered using a 5-pole Butterworth anti-aliasing filter with a cutoff of 30 Hz. The signals are over-sampled 32-times before being averaged to 50 Hz for further noise reduction. The data are then transmitted to the PC via RS-422 serial lines.

Most of the sensors described in the previous section provide analog signals that are digitized by the REMs. The exceptions include the Riegl lasers and the Ashtech and TANS-vector GPS. These instruments transmit their respective digital data directly to the PC via RS-232 lines.

The Ashtech GPS provides the primary time reference for the data acquisition system. The clock utilized by the Ashtech receiver is synchronized with the time transmitted by the GPS satellites. The clock outputs a one pulse per

second signal to the PC. The pulse is also used to synchronize flow of data transmitted to the PC from the REM modules and other sensors.

Data are written to the PC hard disk once per second in three separate files. The first file contains binary data from all *in situ* and remote sensors. The second file contains binary satellite pseudo-range, carrier phase and Doppler data acquired by the Ashtech GPS during flight. The third file contains an ASCII listing of specific times and locations during the flight when the marker switch was toggled to an "on" or "off" position (i.e., to mark specific flight legs, profiles, etc.)

Upon completion of the flight, these files are copied to removable flash disks and transferred to a ground-based PC for post-flight processing.

In addition to the files collected by the N3R data acquisition system, two files are collected from a ground-based GPS of known location and elevation. These data, when combined with GPS data acquired by N3R, are used to generate differentially corrected positions and velocities for the aircraft.

#### 5. POST-FLIGHT DATA PROCESSING

These data pass through a series of post-flight processing programs with each performing a specific task. All programs are written in GNU C and are executed on a PC under a Linux operating system. The following is a brief outline of the processing steps: Raw GPS data from the aircraft and ground station are combined to produce a set of differentially-corrected GPS aircraft positions and velocities. Next, the aircraft data are merged with the differentially corrected GPS data and converted into netCDF format (Rew et al. 1997). Quality control programs are implemented on this data to remove spikes and outliers. Finally, the calibrations are applied, low- and high-rate data are merged, and the winds are computed. During each step time stamps are written in the output file header. These stamps describe when the data were processed and the version of the processing programs. This information is carried through to the final product. Additionally, the marker files are manually edited to reflect special notes regarding the flight and designate special legs for analysis purposes. Fig. 4 contains a flow chart illustrating the steps for data post-processing.

##### 5.1 Differential GPS Corrections

The initial step in post-flight processing calculates positions and velocities using differential GPS techniques. Although the original data from N3R contains positions and velocities, accuracies are coarse. The raw GPS data used in the corrections algorithm contain satellite navigation information and, for each epoch, signal phase, pseudo-range, and satellite number. Based on these data collected from two separate locations, one of which is precisely known (the ground-station), it is possible to calculate very accurate position and speed of the remote observing station (N3R). For this purpose, an algorithm (*flykin*) developed by the Department of Geomatics Engineering at the University of Calgary is used (Cannon et al. 1993). The algorithm uses advanced filtering



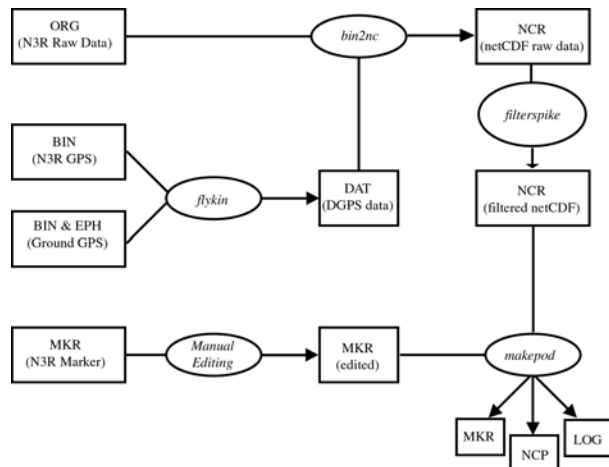


**Fig. 4.** Flowchart illustrating the steps of the N3R post-processing algorithms. Rectangles indicate files, ovals indicate individual programs.

techniques and phase information to resolve ambiguities resulting from the determination of position based solely on pseudo-range. The source code for this software package was provided by the University of Calgary and has been modified by ARL for our application.

### 5.2 NetCDF Conversion

The next step in the data post-processing converts the files from their native format into Network Common Data Format (NetCDF). This program (*bin2nc*) executes a simple file conversion. It also merges output from the differentially corrected GPS data, replacing the uncorrected GPS data stored in the original aircraft files. During the merging process, flags are set for missing GPS data. Also, because data are stored either as short- or long-word integers, a scale factor and offset must be computed. These values are assigned to variable attributes in the NetCDF file.

### 5.3 Quality Control

The next program applies quality control checks on the raw data and apply corrections as necessary. A despiking routine (*filterspike*) checks the data for regions where values fall outside of a prescribed range or are equal to some predefined “fill” value. In these regions, data are linearly interpolated based on the last and next “good” value. After completing the interpolation, flags are set for those regions where data were interpolated.

### 5.4 Final Processing

The final step in the post processing algorithms is to carry through the actual computation of winds, apply recovery factors based on aircraft velocity, and to merge data from slow- and fast-response sensors. A program (*makepod*) calculates winds based on the raw pressure measurements from the BAT probe in combination with data from the GPS. High- and low-frequency measurements of position, velocity, temperature, and

water vapor are blended by first performing Fourier transforms followed by passing the data through appropriate high- and low-pass filters, merging the sets, and finally calculating the inverse transform (Eckman et al. 1999).

Wind calculations use a method similar to the NCAR method described by Leise and Masters (1991). Modifications to the NCAR method result from the unique configuration of the BAT probe in that a reference pressure (not a true static pressure) is provided by the pneumatic average of the four reference pressure ports. Consequently, the dynamic pressure must be corrected not only for variations in attack angle and sideslip, but also for deviations of reference pressure from the static pressure. The computation of accurate wind measurements requires the empirical determination of several probe calibration constants. Of particular interest are the angle offsets, roll, pitch, heading, angle of attack offset, and dynamic pressure adjustment. The values of these constants are determined by minimizing the variance of the three individual wind components for various flight legs. These legs include straight and level flight, dynamic and steady-state pitch and yaw maneuvers, reverse-heading maneuvers, and wind circles and boxes. Theoretically determined constants, based on theory of potential flow over a sphere are also included in the wind calculations. These include attack and sideslip calibration constants and the aircraft upwash factor.

## 6 DATA

There are four files available to users of the N3R data. The *NCR* file is the raw netCDF file that includes only non-calculated quantities (e.g., static pressure, uncorrected temperature, unblended positions and velocities from GPS and accelerometers, etc.). The *NCP* file contain derived quantities (e.g., wind velocity, corrected air temperature and humidity). The structure of the *NCR* and *NCP* files is determined based upon the NetCDF file structure (Rew et al. 1997). Further information on these netCDF libraries can be found at [www.unidata.ucar.edu/packages/netcdf](http://www.unidata.ucar.edu/packages/netcdf). The header of each file contains information relating to the data variables, their dimensions, attributes for each variable, and attributes for the entire file. All of the data are stored either as short-word (4-byte) or long-word (8-byte) integers. All either contain one or two dimensions. The primary dimension for the 1-Hz variables is *scan* which is equal to the number of seconds contained in the file. Higher rate variables (10, 50, or 150 Hz) have a second dimension.

The *MKR* files contain ASCII data listings of specific times and locations during the flight when the marker switch was toggled to an “on” or “off” position. When the marker switch is turned on or off, the time, latitude and longitude are written to the *MKR* file. These marker pairs are used to denote the start and end of flux legs, profiles, or specific maneuvers. An “event” switch is used to mark a single event during flight (e.g., flying over a ship or buoy). The *MKR* file is manually edited at the end of the flight to include a summary of the weather conditions, flight plan, problems encountered, and other notes that may be

helpful during data analysis.

The LOG file contains a listing of input parameters passed through *makepod*. Contained are switches indicating what instruments were on the aircraft and hence what variables exist in the files. Also included are calibration factors for wind calculations. Filter pass and stop bands are recorded in the LOG files. These describe the frequency bands for the high- and low-pass filters used to blend variables. Valid minima and maxima are also defined. Statistics for the raw and processed variables are determined, including minimum, maximum, and moments.

## 7. EXAMPLES

### 7.1 Satellite Altimeter Bias

The wind-sheltered smoother troughs of ocean waves backscatter more electromagnetic (EM) energy emitted by the Topex / Poseidon satellite than the wind-roughened crests (Fig. 5). In addition, a portion of the emitted EM signal is scattered by the wave crests down into the wave troughs. As a result, satellite altimeter data are negatively biased. The magnitude of this bias is a function of various wave characteristics. In general, this bias grows with wave amplitude and speed and can exceed 5% of the significant wave amplitude. N3R was used in the Wave Profile Experiment (WAPLEX) in November 1998 to gather data on ocean wave characteristics in order to reduce the uncertainty of satellite altimeter data acquired by Topex/Poseidon.

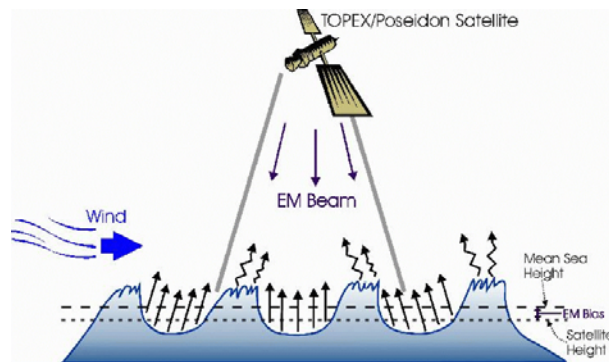


**Fig. 5.** Schematic depicting Topex/Poseidon EM bias.

The solid line in the top graph of Fig. 6 is a probability density function (PDF) of the sea surface elevation as a function of wave height based on the laser altimeter and radar scatterometer data acquired by N3R during a WAPLEX flight leg. The diamonds represent the variance of the wave slope as a function of wave height. These points clearly show that the ocean wave troughs are much smoother (exhibit less variance in wave slope) than the wave crests. The stars represent the mean radar cross-section as a function of wave height. As expected, the backscatter return of the EM signal is significantly greater for wave troughs than for crests. The bottom graph in Fig. 6 is a scatter plot of the wave slope variance as a function of wave height after the short waves have been removed. Again, these data points show less variance in the troughs than the wave crests. For this

particular flight leg, the significant wave height was 1.41 m. The radar altimeter measurements of mean sea level were negatively biased by 1.56% of the significant wave height, which is 2.2 cm (~1 in).

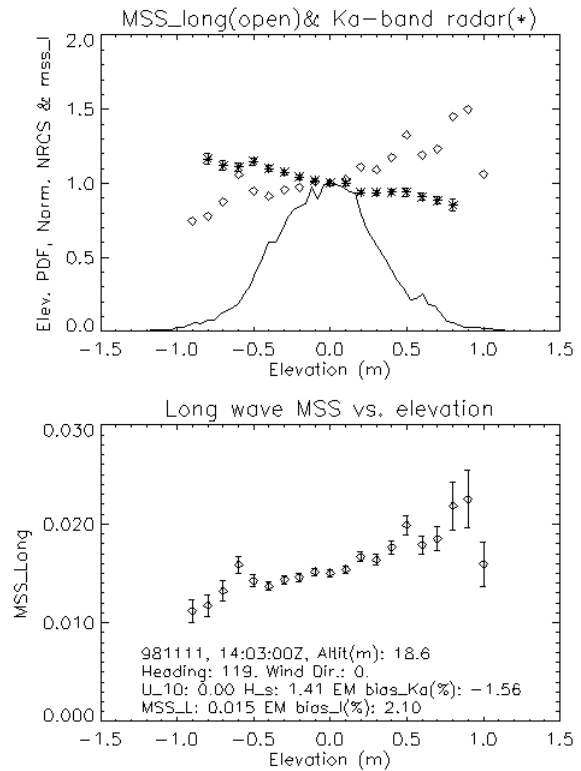


**Fig. 6.** Probability density function (solid line), wave slope variance (diamonds), and mean radar cross section (stars) as a function of wave height (top graph). Mean radar cross section as a function of wave height after removal of short waves (bottom graph).

### 7.2 Atmospheric Roll Vortices

N3R was able to document the response of wind-generated ocean waves by atmospheric forcing (Vandemark et al. 2001). Widespread horizontal roll vortices were present over the Mid-Atlantic Bight during a mild cold-air outbreak 5 November 1997. The mean wind speed was  $7.5 \text{ m s}^{-1}$  from the northeast. The average air temperature was  $9.7^\circ \text{C}$  while the SST varied between  $15$  and  $16^\circ \text{C}$ . The eddy correlation method was used to estimate turbulent fluxes. The sensible, latent, and buoy heat fluxes were  $56$ ,  $64$ , and  $111 \text{ W m}^{-2}$ , respectively, while the friction velocity was  $0.29 \text{ m s}^{-1}$ . The Monin-Obukhov stability parameter was  $z/L$  was estimated to be  $-0.29$ . Vandemark et al. (2001) found that significant variability in the wind field existed at scales below  $3 \text{ km}$  and the total stress was dominated by small-scale turbulent eddies with a spectral peak near  $80$  to  $100 \text{ m}$ .

N3R flew low-level (~15 m) flux legs along and across the mean wind. The average peak length scale for the along-wind velocity for flight legs across the roll vortices was  $1.5 \text{ km}$ . The mss of short waves show the same modulation about the mean as the wind speed (Fig. 7).

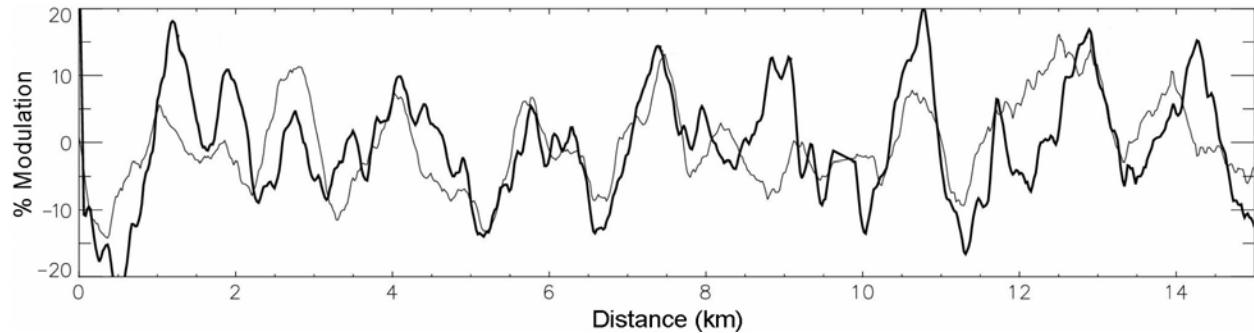


**Fig. 7.** Percent modulation of along-wind velocity (thin line) and mean square slope of short waves for low-level flight leg across horizontal roll vortices on 5 November 1997 off the North Carolina coastline (Vandemark et al. 2001).

These aircraft data provide evidence of the impact of the wind on ocean surface. Higher and lower wind speed almost always equates with increased or decreased slope variance, respectively.

To further illustrate this, the power spectral density of the along-wind velocity and short-wave mss for this same cross-wind flight leg is shown in Fig. 8. The peak wave number of  $0.004 \text{ rad m}^{-1}$  corresponds to a wave scale of  $\sim 1.5 \text{ km}$ . The mean square coherence between the along-wind velocity and short-wave mss is also very high ( $\sim 0.7$ ) for wave scales between 1.5 and 2 km.

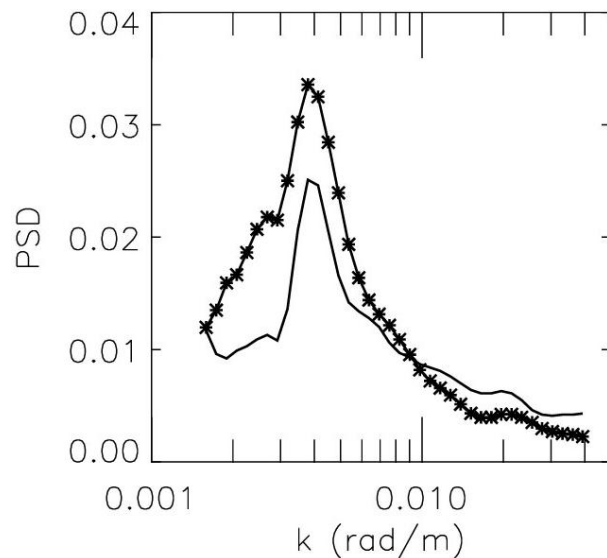


**Fig. 8.** Power spectral density of along-wind velocity (thin line) and short-wave mms (thick line with stars) (Vandemark et al. 2001).

### 7.3 Turbulence in the Coastal Shoaling Zone

Existing parameterizations of the surface wind stress in the coastal shoaling zone usually fail because of their inability to properly account for changes of surface wave characteristics such as height, steepness, period, phase speed, breaking, and age. Accurate model simulation of the surface stress and turbulence above the air-sea interface is important for a number of applications including understanding wave growth and decay. N3R was used off the coast of North Carolina in the Shoaling

Waves Experiment (SHOWEX) to investigate the spatial variation of both marine boundary layer and surface wave field (Crescenti et al. 1999; French et al. 2000).

Mahrt et al. (2001) examine the partial collapse of turbulence in offshore flow of warm air over cooler water. Three offshore zones were determined based on numerous N3R flight. Surface stress and roughness length  $z_0$  decrease rapidly from the coastline out to 2 to 4 km in the near-coastal zone. A quasi-frictional decoupling zone exists out to 10 to 15 km where the stress and  $z_0$  maintain extremely small values. Stress and  $z_0$  increase in the recovery zone at distances greater than 10 to 15 km from the coastline. This behavior in  $z_0$  is shown in Fig. 9.

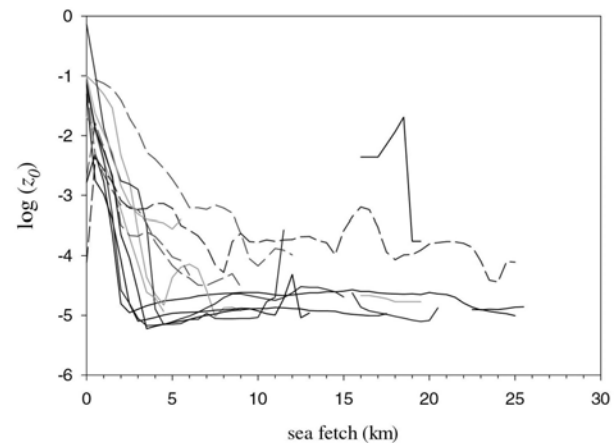


**Fig. 9.** Roughness length as a function of fetch from numerous 10-m N3R flight legs (Mahrt et al. 2001).

The roughness length reach a minimum around  $5 \text{ m s}^{-1}$  which is agreement with results from previous studies (Fig. 10). The dramatic increase in  $z_0$  with decreasing wind speed is due in part to surface tension and wave induced stress associated with swell (Rieder and Smith 1998; Plant et al. 1999). The solid curve in Fig. 10 are for values of  $z_0$  when the stress vector is within  $45^\circ$  of opposing the wind vector. When this criteria is relaxed,  $z_0$  increases by an order of magnitude at very weak wind speeds. Thus, it is likely that the increase in  $z_0$  for very light winds is due to a wave-driven stress. The wave-driven stress is not expected to obey similarity theory but enhances the total stress and therefore the aerodynamic roughness length computed from that stress.

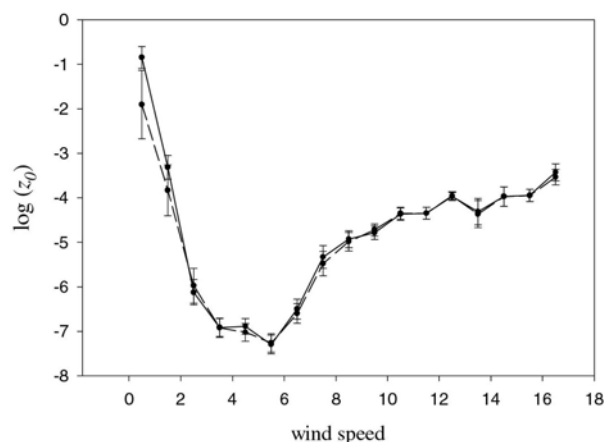


**Fig. 10.** Roughness length as a function of wind speed when stress vector is within 45 deg of wind vector (solid line) and for all cases (dashed line) (Mahrt et al. 2001).

## 8. SUMMARY

The N3R integrated airborne measurement system is capable of acquiring high-fidelity atmospheric turbulence and ocean surface wave field data. N3R is a high-utility aircraft that is an ideal platform to carry state-of-the-science *in situ* and remote sensors. These data are being used to advance our understanding of air-sea interaction.

## 9. ACKNOWLEDGMENTS

This work was supported in part under contracts from the Office of Naval Research (N00014-97-F-0123 and N00014-01-F-0008) and by NOAA's Office of Oceanic and Atmospheric Research. The authors wish to thank our colleagues Sean Burns, Ron Dobosy, Ed Dumas, Rick Eckman, Larry Mahrt, Jielun Sun, and Dean Vickers for their support towards the continued improvement of aircraft-based measurements.

## 10. REFERENCES

- Auble, D. L., and T. P. Meyers, 1992: An open path, fast response infrared absorption gas analyzer for  $H_2O$  and  $CO_2$ . *Bound.-Layer Meteor.*, **50**, 77-108.
- Bowers, J. F., G. E. Start, R. G. Carter, T. B. Watson, K. L. Clawson, and T. L. Crawford, 1995: The Long-Range Overwater Diffusion (LROD) Experiment. *Eleventh Sym. Boundary Layers and Turbulence*, Charlotte NC, Amer. Meteor. Soc., 148-151.
- Cannon, M. E., G. LaChapelle, and G. Lu, 1993: Kinematic ambiguity resolution with a high precision C/A code receiver. *J. Surveying Engin.*, **119**, 147-155.
- Crawford, T. L., and R. J. Dobosy, 1992: A sensitive fast-response probe to measure turbulence and heat flux from any airplane. *Bound.-Layer Meteor.*, **59**, 257-278.
- Crawford, T. L., R. T. McMillen, T. P. Meyers, and B. B. Hicks, 1993: Spatial and temporal variability of heat, water vapor, carbon dioxide, and momentum air-sea exchange in a coastal environment. *J. Geophys. Res.*, **98**, 12869-12880.
- Crawford, T. L., R. J. Dobosy, and E. J. Dumas, 1996: Aircraft wind measurement considering lift-induced upwash. *Bound.-Layer Meteor.*, **80**, 79-94.
- Crescenti, G. H., T. L. Crawford, and E. J. Dumas, 1999: Data report: LongEZ (N3R) participation in the 1999 Shoaling Waves Experiment (SHOWEX) pilot study. NOAA Tech. Memo. ERL ARL-232, Silver Spring, MD, 86 pp.
- Eckman, R. M., T. L. Crawford, E. J. Dumas, and K. R. Birdwell, 1999: Airborne meteorological measurements collected during the Model Validation Program (MVP) field experiments at Cape Canaveral, Florida. NOAA Tech. Memo. OAR ARL-233, Silver Spring, MD, 54 pp.
- French, J. R., G. H. Crescenti, T. L. Crawford, and E. J. Dumas, 2000: LongEZ (N3R) participation in the 1999 Shoaling Waves Experiment (SHOWEX). NOAA Data Rep. OAR ARL-20, Silver Spring, MD, 51 pp.
- French, J. R., T. L. Crawford, R. C. Johnson, and O. R. Cote, 2001: A high-resolution temperature probe for airborne measurements. *Eleventh Symposium on Meteorological Observations and Instrumentation*, Albuquerque, NM, Amer. Meteor. Soc., 139-144.
- Hacker, J. M., and T. L. Crawford, 1999: The BAT-probe: The ultimate tool to measure turbulence from any kind of aircraft (or sailplane). *J. of Technical Soaring*, **XXIII**, 43-46.
- Leise, J. A., and J. M. Masters, 1991: Wind measurement from aircraft. Unpublished Tech. Rep., NOAA Aircraft Operations Center, Miami, FL, 182 pp.
- Mahrt, L., D. Vickers, J. Sun, T. L. Crawford, G. H. Crescenti, and P. Frederickson, 2001: Surface stress in offshore flow and quasi-frictional decoupling. *J. Geophys. Res.*, **106**, in press.
- Mourad, P. D., D. R. Thompson, and D. C. Vandemark, 2000: Extracting fine-scale winds from synthetic aperture radar images of the ocean surface. *John Hopkins APL Tech. Digest*, **21**, 108-115.
- Plant, W. J., D. E. Weissman, W. C. Keller, V. Hessany, K. Hayes, and K. W. Hoppel, 1999: Air/sea momentum transfer and the microwave cross section of the sea. *J. Geophys. Res.*, **104**, 11173-11191.
- Rew, R., G. Davis, S. Emmerson, and H. Davies, 1997: *NetCDF User's Guide for C: An Access Interface for Self-Describing, Portable Data, Version 3*. Unidata Program Center, University Corporation for Atmospheric Research, Boulder CO.
- Rieder, K. F., and J. A. Smith, 1998: Removing wave effects from the wind stress vector. *J. Geophys. Res.*, **103**, 1363-1374.
- Vandemark, D., P. D. Mourad, S. A. Bailey, T. L. Crawford, C. A. Vogel, J. Sun, and B. Chapron, 2001: Measured changes in ocean surface roughness due to atmospheric boundary layer rolls. *J. Geophys. Res.*, **106**, 4639-4654.
- Vogel, C. A., and T. L. Crawford, 1999: Exchange measurements above the air-sea interface using an aircraft. *Air-Sea Exchange: Physics, Chemistry and Dynamics*, G. L. Geernaert, Ed., Kluwer Academic Publishers, 231-245.